eprints@whiterose.ac.uk
https://eprints.whiterose.ac.uk/

The effect of heat treatment on precipitation in the Cu-Ni-Al alloy Hiduron® 130

Katerina A. Christofidou[1], K. Jennifer Robinson[1], Paul M. Mignanelli[1], Edward J. Pickering[2], Nicholas G. Jones[1] and Howard J. Stone[1]

[1]Department of Materials Science and Metallurgy, University of Cambridge, 27 Charles Babbage Road, Cambridge, CB3 0FS, UK

[2] School of Materials, The University of Manchester, Manchester, M13 9PL, UK

Dr. K. A. Christofidou
tel: +44 (0) 1223331950
email: kc424@cam.ac.uk
ORCID: 0000-0002-8064-5874

The effect of heat treatment on precipitation in the Cu-Ni-Al alloy Hiduron® 130

Cupronickel alloys, reinforced by $L1_2$ precipitates, offer a high strength, corrosion resistant and anti-bio fouling material for marine engineering applications. These alloys exhibit complex precipitate nucleation and growth mechanisms that must be fully understood in order to optimise the mechanical properties. In this work, the microstructural characteristics of the Cu-Ni-Al based alloy, Hiduron® 130, have been assessed in the as-received condition and following 100-hour thermal exposures at 500, 600, 700 and 900˚C and after a two-stage exposure at 900˚C for 100hours followed by 500˚C for 100 hours. The $L1_2$ phase was observed to precipitate both discontinuously and continuously and its subsequent coarsening was characterised alongside measurements of the lattice misfit. The hardness of the alloy was found to decrease with increasing exposure temperature up to the $L1_2$ solvus and correlated with the evolution of the $L1_2$ precipitates, the alloy grain size and the fraction of the discontinuously formed $L1_2$ phase.

Keywords: copper alloys; L12 phase; microstructure; SEM; TEM; XRD

Introduction

Precipitate hardened cupronickel alloys possess a combination of properties that makes them ideally suited for highly loaded components in marine engineering. The alloys benefit from superior mechanical properties than binary cupronickel alloys, whilst retaining excellent corrosion resistance in aqueous environments, a low susceptibility to hydrogen embrittlement and stress corrosion cracking, and good anti-biofouling properties [1]. Furthermore, recent research has identified Cu-Ni-Al alloys as possible replacements for precipitate hardened Cu-Be alloys used in electronics applications on account of the toxicity of Be [2-4].

High strength cupronickel alloys may be realised through Al additions to Cu-Ni binary alloys, which provides age hardening through the formation of $L1_2$

(Strukterbericht notation) precipitates, analogous to the well-known γ' particles found in Ni-based superalloys [5]. Precipitation of the $L1_2$ phase in cupronickel alloys provides a large improvement in the mechanical properties, not only through conventional precipitation hardening mechanisms, but also as a result of the ordered nature of the precipitates and their crystallographic similarity to the A1 matrix in which they reside. The passage of a/2<-110> dislocations from the A1 matrix into the ordered $L1_2$ phase encounters increased resistance, due to the energy penalty associated with the formation of an anti-phase boundary created in the $L1_2$ structure, which can only be reduced by the passage of a second dislocation through the precipitate [6-8].

Previous studies have reported on the microstructural characteristics and $L1_2$ precipitation behaviour of Cu-Ni-Al alloys [4,9-12], the effect of thermomechanical treatments on the alloy properties and microstructure [2,10,13,14] as well as the effect of additional alloying elements [2,10,15]. Precipitation of the $L1_2$ phase in Cu-Ni-Al alloys occurs through both continuous and discontinuous processes, whereas, for alloys with high concentrations of Al, the B2 – NiAl phase may also precipitate [5,9-11,13,14]. The discontinuous precipitation of the $L1_2$ phase, as well as the formation of the B2 phase, will result in the weakening of the alloy through the consumption of Al, leading to a reduction in the volume fraction of the continuously precipitated $L1_2$ phase.

Several compositions of Cu-Ni-Al-based alloys have been studied with the aim of determining the optimal thermomechanical processing route, and in particular, the optimum $L1_2$ precipitate size required to maximise the mechanical properties [11,12,14,16]. Whilst these studies presented a very thorough characterisation of the evolution of the continuous distributions of the $L1_2$ phase at ~500°C with varying exposure lengths, the effect of different exposure temperatures is not well understood. In addition, although discontinuously precipitated colonies of the $L1_2$ phase have been

reported to occur, the driving force for this precipitation phenomenon is not well documented.

Consequently, this work aims to contribute towards an improved understanding of both the continuous and discontinuous precipitation behavior in the commercially available Cu-Ni-Al alloy, Hiduron® 130. The distribution of the $L1_2$ precipitates and the lattice misfit in the alloy were studied with respect to the exposure temperature. In addition, the hardness of the material following ageing was measured and correlated to the microstructural observations.

Experimental

The chemical composition of Hiduron® 130, as provided by Langley Alloys, is shown in Table 1. The liquidus, solidus and $L1_2$ solvus temperatures were determined using differential scanning calorimetry (DSC), with a 5 mm diameter disc cut from a 1 mm thick slice of the as-received material. Calorimetric data was acquired using a Netzsch 404 calorimeter with an argon atmosphere and a heating/cooling rate of $10°C$ min^{-1}. Heat treatment of the alloy was performed in argon-backfilled quartz ampoules and exposed for 100 hours at temperatures of 500, 600, 700 and 900°C. An additional two-stage exposure at 900°C for 100 and 500°C for 100 hours was also performed. All samples were air cooled from the exposure temperature.

Samples for scanning electron microscopy (SEM) were prepared following standard metallographic preparation techniques. Final polishing of the samples was achieved using a neutral solution of 0.06 μm colloidal silica in H_2O_2. An FEI Nova NanoSEM 450 equipped with a Bruker XFlash 6 solid-state energy dispersive X-ray spectroscopy (EDX) detector was used for the microstructural analysis.

Samples for transmission electron microscopy (TEM) analysis, were prepared as discs 3 mm in diameter and 100 μm thick from as-received material before thinning

using a Gatan 691 Precision Ion Polishing System. Final polishing was performed using a 5 eV argon beam for 30 minutes, followed by a 1 eV beam for 30 minutes. TEM investigations were carried out on an FEI Tecnai Osiris microscope operated at 200 kV and equipped with FEI Super-X EDX detectors. An average particle size distribution was obtained from the microstructural images using the ImageJ software package.

X-ray diffraction (XRD) patterns were collected from 20-120° 2θ on a Bruker D8 diffractometer using Ni-filtered Cu-Kα radiation. To obtain the lattice parameters of the phases present in the structure, the diffraction spectra were fitted using the Pawley method [17] in the TOPAS-academic software package. The lattice misfit (δ) between the Cu-rich A1 matrix and the $L1_2$ precipitates was calculated from the lattice parameters using equation (1).

Equation 1
$$\delta = 2 \left[\frac{a_{\gamma'} - a_{\gamma}}{a_{\gamma'} + a_{\gamma}} \right]$$

The hardness of the material in each condition was evaluated using a Vickers hardness indenter operated with an applied load of 20 kg and a dwell time of 30 s. Ten measurements were obtained from each sample, which were averaged to provide a mean value of hardness.

Results

Microstructural characterisation of as-received Hiduron® 130

Understanding the microstructure of the as-received material was vitally important for tracking the evolution of the alloy microstructure following the thermal exposures. Figure 1 presents backscattered electron images of the key features observed in the alloy in the as-received state. The grain structure of the material is shown in Figure 1a, from

which the average grain size was found to be $\sim 14 \pm 5$ μm in diameter. Closer examination also revealed regions of discontinuous precipitation and the formation of discrete dark particles at the grain boundaries, as shown in Figures 1b and 1c. However, the $L1_2$ particles were not observed at this length scale, hence, TEM-based techniques were utilised to confirm the presence of nanosized $L1_2$ precipitates.

Figure 2 presents the collective results from the TEM analyses; Figure 2a shows a high angle annular dark field (HAADF) scanning transmission electron microscopy (STEM) image of the bulk material, and is accompanied by EDX maps of the key elements in the alloy: Ni, Fe, Al and Cu, shown in Figure 2b-e respectively. The EDX results indicated that Cu was the principal constituent of the A1 matrix whilst Ni and Al preferentially partitioned to the $L1_2$ precipitates. Fe also displayed preferential partitioning towards the $L1_2$ phase, but to a lesser extent than Ni and Al. Figure 2f shows the electron diffraction pattern from a typical region of the material in which fundamental reflections from the A1 matrix were observed, along with superlattice reflections indicative of the presence of the $L1_2$ phase. A dark field image obtained from the (100) superlattice reflection is included in Figure 2f in which the $L1_2$ precipitates may be clearly discerned. Using data from both the STEM and dark field images, the $L1_2$ phase was found to form in a spherical morphology with an average diameter of 18 ± 6 nm.

As stated previously, in addition to $L1_2$ precipitation, the formation of discrete grain boundary particles and discontinuously precipitated colonies were observed in the alloy. HAADF STEM images and EDX maps of the discontinuously formed $L1_2$ and A1 phases are shown in Figure 3. Whilst reliable diffraction patterns could not be obtained from the phases present, the relative partitioning behavior of the elements was indicative of their nature. In Figure 3b-e, the discontinuously formed lamellar

precipitates exhibited similar elemental partitioning behavior to that observed in the spherical $L1_2$ precipitates i.e. Cu was found to strongly partition towards the matrix, whereas Ni, Al and to a lesser extent Fe, partitioned preferentially towards the discontinuous aggregates. Hence, these precipitates were also believed to form with the $L1_2$ structure and are separated by the A1 phase.

Differential scanning calorimetry

A thermogram of the first heating cycle of the as-received material is shown in Figure 4 in which the transition temperatures have been marked. The liquidus, solidus and $L1_2$ solvus temperatures were found to be 1180˚C, 1110˚C and 825˚C respectively. Guided by these data three sub-solvus heat treatment temperatures were selected at 500, 600 and 700˚C, and one super-solvus heat treatment temperature of 900˚C to investigate the evolution of the microstructure after thermal exposure above and below the γ′ solvus.

Microstructural characterisation following thermal exposures

Following the thermal exposures of the material, SEM was used in order to understand the microstructural evolution of the samples as a function of temperature, Figure 5. The material exposed at 500˚C, Figure 5a & b, displayed only marginal coarsening of the discontinuously precipitated colonies, whilst further microstructural changes were not observed. Increasing the thermal exposure temperature to 600˚C led to a dramatic coarsening of the discontinuously precipitated colonies, which were observed to decorate most grain boundaries in the structure, Figure 5c. In addition, significant coarsening of the intergranular $L1_2$ precipitates was also observed, Figure 5d. The material exposed at 700˚C displayed a very similar behaviour to the material exposed at 600˚C, although the kinetics of coarsening were much faster, leading to an average $L1_2$ size of 120 ±40 nm, Figure 5e & f. In addition to the growth of the $L1_2$ precipitates, a

transition in the morphology of the precipitates from spherical to cuboidal was observed in the samples exposed to 600 and 700˚C. Whilst the sub-solvus heat treatments were found to significantly influence the microstructural evolution of the $L1_2$ precipitates, the grain structure of the material in all sub-solvus conditions remained largely unchanged, with an average grain size comparable to the material in the as-received condition. In contrast, the samples exposed at 900˚C, Figure 5 g & h, and at 900˚C for 100 hours followed by 500˚C for 100 hours, Figure 5 i & j, displayed considerable grain coarsening, resulting in an average grain diameter that exceeded 100 µm. Whilst, no bulk phases were observed in the samples at this length scale, the precipitation of fine, nano-scale $L1_2$ precipitates is expected to have occurred on cooling from the 900˚C exposure. In addition, a small fraction of discontinuously precipitated $L1_2$ phase, which leads to the serrated morphology of the grain boundaries, was also observed. As with the sample exposed to 500˚C for 100 hours, the sample subjected to 900˚C for 100 hours followed by 500˚C for 100 hours exhibited marginal coarsening of the discontinuously precipitated products. Importantly, the discrete, grain boundary pinning precipitates observed as the dark phase in the as-received material could not be identified in any of the heat-treated samples examined.

X-ray Diffraction

The evolution of the microstructure, and in particular the A1 and $L1_2$ phases, was also investigated using laboratory XRD in the as-received condition and following each thermal exposure. Figure 6a presents a subsection of the data obtained from the material exposed at 600˚C for 100 hours and is overlaid with the fit produced using the Pawley procedure. The Pawley method was used to analyse the results due to the flexibility it allows for fitting the intensity of the peaks [17]. Whilst the material did not display preferential orientation or texture, little information was known about the compositions

of the phases and their relative volume fraction, and hence, the Rietveld method could not be reliably applied. The patterns obtained from all samples were found to only comprise contributions from the A1 and $L1_2$ phases. The lattice parameters obtained for each phase as a function of heat treatment temperature are shown in Figure 6b, and the lattice misfit calculated from these results is displayed in Figure 6c. Upon closer examination of the results, it was observed that the A1 lattice parameter remained largely unchanged, only varying ~ 0.01Å over the range of heat treatments. In contrast, the lattice parameter of the $L1_2$ phase decreased from ~3.611 ±0.001 Å in the as-received state, to ~3.597 ±0.001 Å following thermal exposure at 700˚C. The lattice parameters of the phases in the sample exposed to the $L1_2$ super-solvus heat treatment at 900˚C were comparable to the material in the as-received state. In contrast, the lattice parameters of both phases in the material exposed to the two-stage heat treatment (900˚C for 100 hours and 500˚C for 100 hours), were found to be lower than the lattice parameters obtained in the material exposed to 500˚C for 100 hours, with a larger decrease observed in the lattice parameter of the $L1_2$ phase than that of the A1 phase.

These results were also reflected in the calculations of the lattice misfit between the phases. Using Equation 1, the lattice misfit was found to be negative for the material in all conditions, consistent with the observations that the A1 lattice parameter remained larger than the $L1_2$ lattice parameter. However, a large variation in the magnitude of the lattice misfit was found, which was initially -0.2% and steadily increased to -0.67% at 700˚C. As expected, the lattice misfit was restored to a magnitude of -0.27% when subjected to the super-solvus heat treatment at 900˚C, consistent with the dissolution and re-precipitation of the $L1_2$ phase with a similar chemistry to the as received material.

Hardness

To assess the effects of the microstructural changes on the strength of the material, hardness measurements were completed following each heat treatment and the results are shown in Figure 7. The as-received material exhibited a hardness of 273 ±7 Hv. This increased to 294 ±3 Hv following thermal exposure at 500˚C for 100 hours. However, at higher temperatures the hardness of the material decreased significantly, to a minimum value of 183 ±2 Hv following the heat treatment at 700˚C. The super-solvus heat treatment at 900˚C produced a higher hardness value of 255 ±5 Hv that increased further following the additional heat treatment at 500˚C for 100 hours to 291 ±6 Hv.

Discussion

The material in the as-received state (Figure 1) had a mean grain size of 14 μm, and exhibited a significant fraction of annealing/recrystallisation twins. A continuous nanosized distribution of $L1_2$ particles was found to precipitate intragranularly, whilst, discontinuously precipitated colonies of the $L1_2$ phase and discrete precipitates were found along the grain boundaries. The precipitation of intermetallic phases through discontinuous processes has been extensively reported in alloys based on Cu [18,19], and the occurrence of such reactions in Cu-Ni-Al alloys has also been investigated [10,11,13,14]. However, the driving force for the precipitation of the $L1_2$ phase through a discontinuous process in Cu-Ni-Al alloys is not well understood. It is generally accepted that discontinuous precipitation occurs when the composition of the solid solution is supersaturated in a particular component and continuous precipitation is kinetically unfavourable [19]. In such cases, the supersaturated solid solution isothermally decomposes into lamellar aggregates along high angle grain boundaries that act as paths of fast diffusion. Stored strain energy due to prior deformation may

also contribute to the initiation of the discontinuous reaction. In the case of Cu-Ni-Al alloys, such as Hiduron® 130, the driving force for discontinuous precipitation is believed to be derived from the limited solubility of Al in the Cu solid solution, which for concentrations of Ni between 10-20 at.% was found to be ~0.1-0.8 at.% Al [5]. This hypothesis is further strengthened by the observations of Sierpiński et al. [10], who showed the absence of discontinuously precipitated colonies in Cu-Ni-Al alloys slowly cooled from 900˚C to 500˚C. Slow cooling allowed the elemental redistribution by diffusion required for the continuous precipitation of the L1$_2$ phase. As a result, the growth of the discontinuous precipitates is likely to be governed by the grain boundary diffusion of either Ni or Al [20].

In addition to the distinct discontinuously precipitated colonies found in the material and presented in Figures 1b and 3a-e, the precipitation of the dark coloured discrete particles shown in Figure 1c, may also have occurred through a discontinuous reaction. The characteristic pinning of the boundary by near-equidistant precipitates was believed to be due to the initiation of the discontinuous reaction through the precipitation of aggregates on a migrating boundary [19,21]. This mechanism of discontinuous precipitation is known to occur when the prior boundary displays a slight curvature that provides the driving force for the initial migration of the boundary. The precipitating phase then forms as a result of the accumulation of solute at the migrating boundary. Subsequently, pinning of the boundary occurs and an additional driving force for the migration of the boundary exists due to the compositional gradient that develops [19-22]. However, as specific compositions or selected area diffraction patterns could not be obtained from either the discontinuous colonies or the pinning precipitates, no further evidence exists to conclusively confirm the nature of these precipitates.

Exposure of the material for 100 hours to the three temperatures below the $L1_2$ solvus temperature, 500, 600 and 700°C, resulted in coarsening of both the continuous and discontinuous precipitate distributions. Coarser microstructures were obtained for the material aged at higher temperatures, which was consistent with a diffusion-controlled process. The driving force for the coarsening of the discontinuous precipitates was believed to be a combination of the remnant supersaturation and the stored elastic energy in the system [19,23]. In contrast, the coarsening of coherent, continuous particle distributions is generally controlled by the lattice misfit between the phases that influences the elastic strain energy and interfacial energy in the material, allowing for a more mobile interface as a result of the higher density of interfacial dislocations [24-28]. In addition, the coherency strains associated with the lattice misfit are also known to impact upon the morphology and preferential alignment of the precipitates, with increasing lattice misfit resulting in the transition from spherical to cuboidal precipitates [24,26,29]. The experimental findings support these theories, as shown through the correlation of the results presented in Figure 5 and 6c. However, ultimately, the size to which the precipitates can grow is theorised to be limited by the overlap of diffusion fields of adjacent particles (soft impingement) and by lattice strains caused by a high volume fraction of precipitates [24].

These microstructural changes were found to have a strong effect on the observed hardness of the material, Figure 7. The alloy was found to achieve peak hardness following ageing at 500°C for 100 hours, but near-linear softening was observed upon ageing at 600 and 700°C. These observations were found to be dependent on the distribution of continuously precipitated $L1_2$ phase. Generally, in precipitation-hardened alloys, particle shearing occurs while the particles are small, whereas dislocations bow around bigger particles. However, if the precipitating phase

forms a superstructure of the matrix, additional energy barriers are introduced due to the ordered nature of the precipitate, and hence, deformation is achieved through the movement of superpartial dislocations [6-8,30]. Consequently, the optimum precipitate size is defined not at the transition from dislocation cutting to bowing, but instead at the transition from weakly coupled to strongly coupled superdislocations [8,31-33]. In order to determine the theoretical optimum precipitate size, the equations for weak and strong coupling, as derived by Brown and Ham [34] and Kozar et al. [35], were used. Equation 2 [35] was used for weakly coupled dislocations, whereas Equation 3 [34] shows the expression for strongly coupled dislocations.

Equation 2
$$\Delta\tau = \frac{1}{2}\left(\frac{\gamma_{\mathrm{APB}}}{b}\right)^{\frac{3}{2}}\left(\frac{bd^*f}{T}\right)^{\frac{1}{2}}A - \frac{1}{2}\left(\frac{\gamma_{\mathrm{APB}}}{b}\right)f$$

Equation 3
$$\Delta\tau = \frac{1}{2}\left(\frac{Gb}{d^*}\right)f^{\frac{1}{2}}0.72w\left(\frac{\pi d^*\gamma_{\mathrm{APB}}}{wGb^2} - 1\right)^{\frac{1}{2}}$$

For both equations: γ_{APB} denotes the APB energy of the $L1_2$ precipitates; b denotes the magnitude of the Burger's vector of the dislocations; d^* describes the critical precipitate size; f the volume fraction of precipitates; T the line tension, which is taken to be equal to $Gb^2/2$ for screw dislocations; A is a geometrical factor equal to 0.72 for spherical precipitates; G is the shear modulus of the material and w is a factor describing the dislocation repulsion and approximated to 1 following Hüther et al. [36]. Several estimations of the quantities used in Equations 2 & 3 were required. The γ_{APB} energy was calculated using the Miodownik and Saunders approach [37] and was found to be ~160 mJ mm^{-2}, averaged over the conditions examined. The Burger's vector was

assumed to be of the a/2[110] type, with a taken to be the lattice parameter of the precipitate obtained through X-ray diffraction measurements of 3.6 Å on average. The shear modulus of the material was taken to be 5.2×10^{10} Pa, as detailed on the specification for the material provided by Langley Alloys [38]. As an estimation of the volume fraction of precipitates in the material could not be unambiguously determined, it was varied from 10% to 50% from which it was determined that the optimum precipitate size was calculated to vary from 34.8 – 48.6 nm. However, it should be noted that the various quantities in the equations are expected to change with temperature and that, therefore, the optimum precipitate size will be dependent upon these changes.

The experimental results showed that the greatest strength was observed following the ageing treatment at 500˚C, although the L1$_2$ precipitate size could not be deduced from image analysis of the backscattered electron images obtained. However, it is likely that this microstructural state benefits from L1$_2$ precipitates with sizes closest to the strong-weak dislocation coupling transition. This is supported by the observation that the average L1$_2$ precipitate size was ~18 nm in the as-received material which falls within the weakly coupled dislocation regime, whereas in the samples exposed at 600 and 700˚C the precipitate sizes were in excess of ~50 nm, leading to strong dislocation coupling or Orowan looping. The L1$_2$ precipitate size for the material exposed at 900˚C was expected to be equivalent to the average size obtained in the as-received material as the L1$_2$ phase re-precipitated upon cooling, and hence, the small decrease in hardness observed after exposure at 900˚C was believed to be due to the observed grain growth.

Interestingly, the hardness of the material exposed to the two-stage heat treatment (900˚C for 100 hours followed by 500˚C for 100 hours) was found to be similar to that of the sample heat treated at 500˚C for 100 hours despite having a larger

grain size. This is believed to be primarily due to the reduced fraction of discontinuously-formed products observed at the grain boundaries, which are believed to reduce grain boundary strength. In addition, as the discontinuous products have been shown to form with the $L1_2$ structure, a reduced fraction of the discontinuous phase could lead to an increase in the fraction of the more potent, continuous $L1_2$ phase within the bulk of the grains, hence leading to improved hardness.

Conclusions

The microstructure of the commercially available, $L1_2$ strengthened, Cu-Ni-Al alloy Hiduron® 130 was characterised using a combination of SEM, TEM and XRD, in the as-received state and following heat treatments at 500, 600, 700 and 900˚C for 100 hours. The microstructure of the material in the as-received state was found to consist of a continuously precipitated distribution of $L1_2$ particles with a mean diameter of ~18 nm, as well as two distinct populations of discontinuously precipitated colonies, both believed to be variants of the $L1_2$ structure. Coarsening of the continuous distribution of $L1_2$, as well as the discontinuous colonies, was observed to occur following the three heat treatments performed at temperatures below the $L1_2$ solvus. The lattice misfit between the Cu-rich matrix and the $L1_2$ phase was found to be the primary driving force for the coarsening of the precipitate distributions. However, the discontinuous colonies served to pin the grain boundaries and hence, no significant grain growth was observed. In contrast, the samples exposed at 900˚C (super-solvus) and at 900˚C for 100 hours followed by 500˚C for 100 hours, displayed significant grain growth, and discontinuous precipitation was suppressed. The hardness of the material was found to be dominated by the microstructural features observed and particularly on the particle size of the continuous distribution of $L1_2$ precipitates. Peak

hardness was attained following the heat treatment at 500˚C for 100 hours and the two-stage heat treatment (900˚C for 100 hours followed by 500˚C for 100 hours), which were believed to form precipitates of a size close to the transition from weak to strong dislocation coupling, calculated to be in the range from 34.8 – 48.6 nm. For the material exposed to the two-stage heat treatment, a reduction in hardness due to the increase in average grain size was offset through the improved hardness offered by a reduction in the discontinuous precipitation along the grain boundaries, which is believed to lead to a commensurate increase in the intragranular $L1_2$ phase fraction.

Acknowledgements

References

[1]   M.S. Parvizi, A. Aladjem, J.E. Castle, Behaviour of 90–10 cupronickel in sea water, International Materials Reviews. 33 (1988) 169–200. doi:10.1179/imr.1988.33.1.169.

[2]   L. Shen, Z. Li, Z. Zhang, Q. Dong, Z. Xiao, Q. Lei, et al., Effects of silicon and thermo-mechanical process on microstructure and properties of Cu–10Ni–3Al–0.8Si alloy, Materials & Design. 62 (2014) 265–270. doi:10.1016/j.matdes.2014.04.053.

[3]   L. Shen, Z. Li, Q. Dong, Z. Xiao, C. Chen, Microstructure and texture evolution of novel Cu-10Ni-3Al-0.8Si alloy during hot deformation, Journal of Materials Research. 31 (2016) 1113–1123. doi:10.1557/jmr.2016.104.

[4]   L. Shen, Z. Li, Q. Dong, Z. Xiao, S. Li, Q. Lei, Microstructure evolution and quench sensitivity of Cu-10Ni-3Al-0.8Si alloy during isothermal treatment, Journal of Materials Research. 30 (2015) 736–744. doi:10.1557/jmr.2015.12.

[5]   A. Prince, Aluminium-Copper-Nickel, in: Ternary Alloys, 1991: pp. 597–629.

[6]   A. Cottrell, Dislocations and plastic flow in crystals, Second, Oxford University Press, 1956.

[7]   A. Cottrell, Theoretical Structural Metallurgy, Second, Edward Arnold Ltd, 1955.

[8]   D.P. Pope, S.S. Ezz, Mechanical properties of Ni 3 AI and nickel-base alloys with high volume fraction of γ', International Materials Reviews. 29 (1984) 136–167. doi:10.1179/imr.1984.29.1.136.

[9]   J.P. Stobrawa, Z.M. Rdzawski, Precpitation process of the Ni_3Al phase in copper-based alloys, Journal of Achievements in Materials and Manufacturing Engineering. 15 (2006).

[10]   Z. Sierpiński, J. Gryziecki, Phase transformations and strengthening during ageing of CuNi10Al3 alloy, Mater Sci Eng A. 264 (1999) 279–285.

doi:10.1016/s0921-5093(98)01083-1.

[11] R.J. Grylls, C.D.S. Tuck, M.H. Loretto, Strengthening of a cupronickel alloy by an ordered L12 phase, Intermetallics. 4 (1996) 567–570. doi:10.1016/0966-9795(96)00050-7.

[12] M. Miki, Y. Amano, Aging Characteristics of Cu-30%Ni-Al Alloys, Trans JIM. 20 (1979) 1–10. doi:10.2320/matertrans1960.20.1.

[13] Y.-R. Cho, Y.-H. Kim, T.D. Lee, Precipitation hardening and recrystallization in Cu-4% to 7% Ni-3% Al alloys, Journal of Materials Science. 26 (1991) 2879–2886. doi:10.1007/BF01124816.

[14] H. Tsuda, T. Ito, Y. Nakayama, The improvement of microstructures and mechanical properties in CuNiAl alloys by two-step ageing, Scripta Metallurgica. 20 (1986) 1555–1559. doi:10.1016/0036-9748(86)90394-7.

[15] M. Raghavan, Formation of γ' and γ'' precipitates in Cu-Ni-Nb-Al alloys, Metall Trans A. 9 (1978) 734–736.

[16] J.P. Stobrawa, Z.M. Rdzawski, Precipitation process of the Ni_3Al phase in copper-based alloys, Journal of Achievements in Materials and Manufacturing Engineering. 15 (2006) 21–26.

[17] G.S. Pawley, IUCr, Unit-cell refinement from powder diffraction scans, Journal of Applied Crystallography. 14 (1981) 357–361. doi:10.1107/S0021889881009618.

[18] I. Manna, S.K. Pabi, W. Gust, Discontinous precipitation in a Cu-12 at.% in alloy, Acta Metallurgica Et Materialia. 39 (1991) 1489–1496. doi:10.1016/0956-7151(91)90234-r.

[19] I. Manna, S.K. Pabi, W. Gust, Discontinuous reactions in solids, International Materials Reviews. 46 (2001) 53–91. doi:10.1179/095066001101528402.

[20] R.A. Fournelle, Discontinuous coarsening of lamellar cellular precipitate in an austenitic Fe-30 wt.%Ni-6 wt.%Ti alloy—II. Growth kinetics, Acta Metallurgica. 27 (1979) 1147–1155. doi:10.1016/0001-6160(79)90132-9.

[21] D.B. Williams, E.P. Butler, Grain boundary discontinuous precipitation reactions, International Materials Reviews. 26 (1981) 153–183. doi:10.1179/imr.1981.26.1.153.

[22] F. Findik, Discontinuous (cellular) precipitation, J Mater Sci Lett. 17 (1998) 79–83.

[23] J.D. Livingston, J.W. Cahn, Discontinuous coarsening of aligned eutectoids, Acta Metallurgica. 22 (1974) 495–503. doi:10.1016/0001-6160(74)90103-5.

[24] R.A. Ricks, A.J. Porter, R.C. Ecob, The growth of γ' precipitates in nickel-base superalloys, Acta Metallurgica. 31 (1983) 43–53. doi:10.1016/0001-6160(83)90062-7.

[25] A.J. Porter, R.C. Ecob, R.A. Ricks, Coherency strain fields: magnitude and symmetry, Journal of Microscopy. 129 (1983) 327–336. doi:10.1111/j.1365-2818.1983.tb04189.x.

[26] A.J. Ardell, The effects of elastic interactions on precipitate microstructural evolution in elastically inhomogeneous nickel-base alloys, Philosophical Magazine. 94 (2014) 2101–2130. doi:10.1080/14786435.2014.906756.

[27] A. Baldan, Progress in Ostwald ripening theories and their applications to nickel-base superalloys. Part I: Ostwald ripening theories, Journal of Materials Science. 37 (2002) 2171–2202.

[28] A. Baldan, Progress in Ostwald ripening theories and their applications to nickel-base superalloys. Part II: Nickel-base superalloys, 37 (2002) 2379–2405.

[29] A.J. Ardell, The growth of gamma prime precipitates in aged Ni−Ti alloys,

Metall and Mater Trans B. 1 (1970) 525–534. doi:10.1007/BF02811564.

[30]   R.C. Reed, The Superalloys, Cambridge University Press, Cambridge, 2006.

[31]   B. Reppich, Some new aspects concerning particle hardening mechanisms in γ' precipitating Ni-base alloys—I. Theoretical concept, Acta Metallurgica. 30 (1982) 87–94. doi:10.1016/0001-6160(82)90048-7.

[32]   B. Reppich, P. Schepp, G. Wehner, Some new aspects concerning particle hardening mechanisms in γ' precipitating nickel-base alloys—II. Experiments, Acta Metallurgica. 30 (1982) 95–104. doi:10.1016/0001-6160(82)90049-9.

[33]   A.J. Ardell, Precipitation hardening, Metall Trans A. 16 (1985) 2131–2165. doi:10.1007/bf02670416.

[34]   L.M. Brown, R.K. Ham, Strengthening Mechanisms in Crystals, Elsevier Publishing company Ltd, London, 1971.

[35]   R.W. Kozar, A. Suzuki, W.W. Milligan, J.J. Schirra, M.F. Savage, T.M. Pollock, Strengthening Mechanisms in Polycrystalline Multimodal Nickel-Base Superalloys, Metall Mater Trans A. 40 (2009) 1588–1603. doi:10.1007/s11661-009-9858-5.

[36]   W. Hüther, B. Reppich, Order Hardening of Mgo by Large Precipitated Volume Fractions of Spinel Particles, Materials Science and Engineering. 39 (1979) 247–259. doi:10.1016/0025-5416(79)90063-6.

[37]   A.P. Miodownik, N.J. Saunders, The calculation of APB energies in $L1_2$ compounds using a thermodynamic data base, in: P. Nash, B. Sundman (Eds.), Applications of Thermodynamics in the Sunthesis and Processing of Materials, 1995: pp. 1–14.

[38]   Langley Alloys Ltd, HIDURON 130: A very high strength cupronickel, 2008.

Table 1: The chemical composition of Hiduron® 130, as provided by Langley Alloys.

Element	Cu	Ni	Al	Fe	Mn	Trace elements
wt%	81.7	14.4	2.7	0.8	0.3	0.1
at%	77.9	14.8	6.0	0.9	0.3	0.1

Figure 1: Back scattered electron images of Hiduron® 130 in the as-received state. a) Grain structure, b) discontinuously precipitated colonies and c) grain boundary pinning particles.
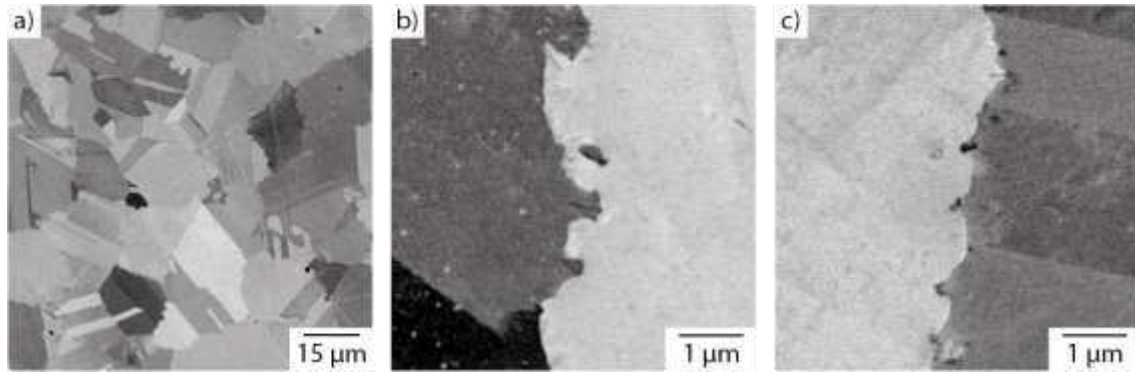
Figure 2: a) HAADF STEM image of the L1$_2$ precipitates in the as received condition b-e) corresponding EDX maps from the Ni, Fe, Al and Cu K-lines and f) dark field image formed from the (100) superlattice reflection of the L1$_2$ precipitates and the equivalent electron diffraction pattern inset.
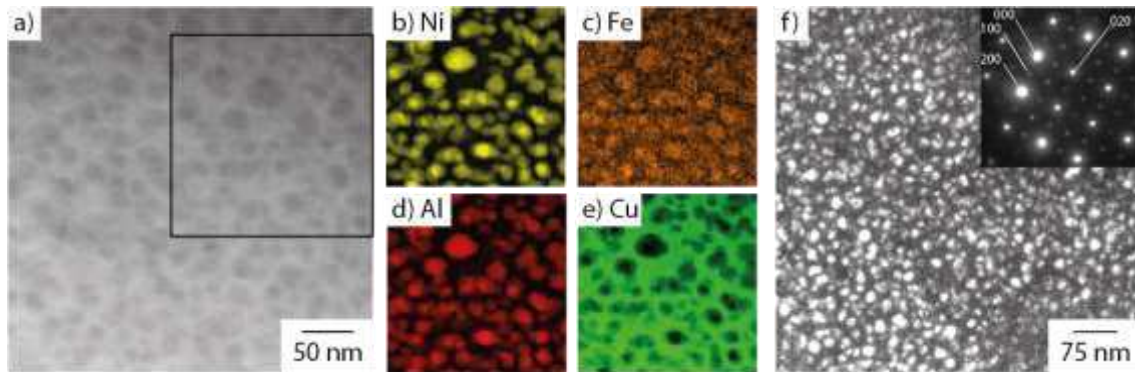
Figure 3: a) HAADF STEM image of a discontinuously formed colony in the as received, b-e) corresponding EDX maps from the Ni, Fe, Al and Cu K-lines (respectively).
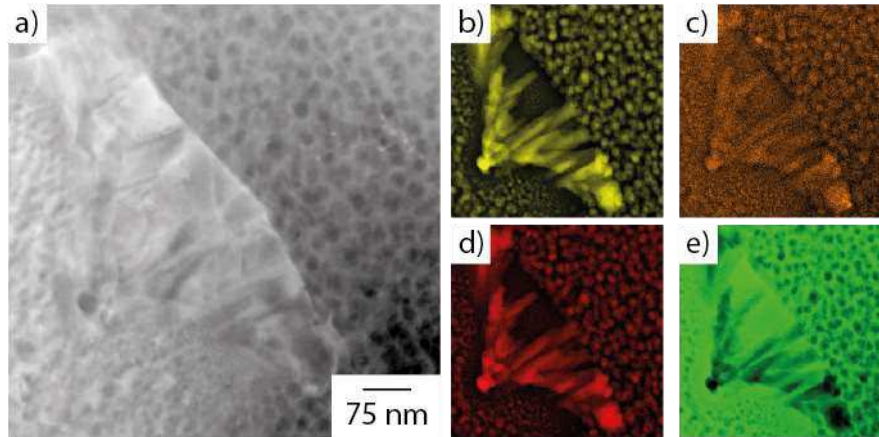
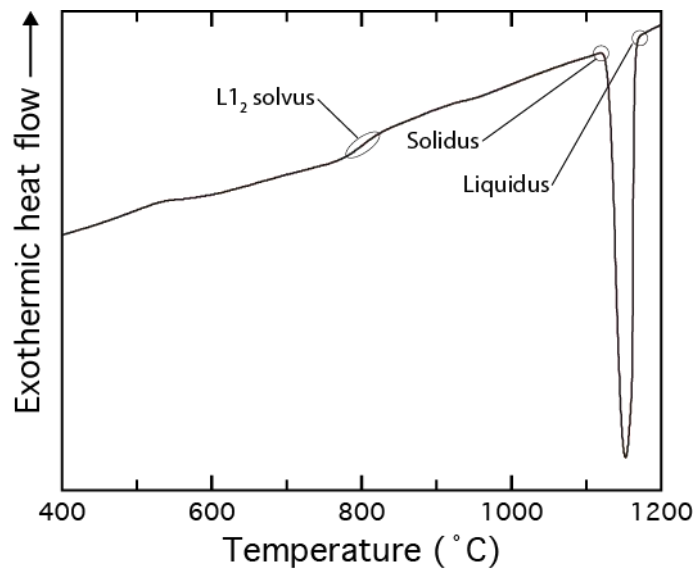Figure 4: DSC heating thermogram of the as-received Hiduron® 130 sample.

Figure 5: Backscattered electron images, at both low and higher magnifications, following thermal exposure for 100 hours at a & b) 500˚C, c & d) 600˚C, e & f) 700˚C, g & h) 900˚C and i & j) 900˚C for 100 hours followed by 500˚C for 100 hours.
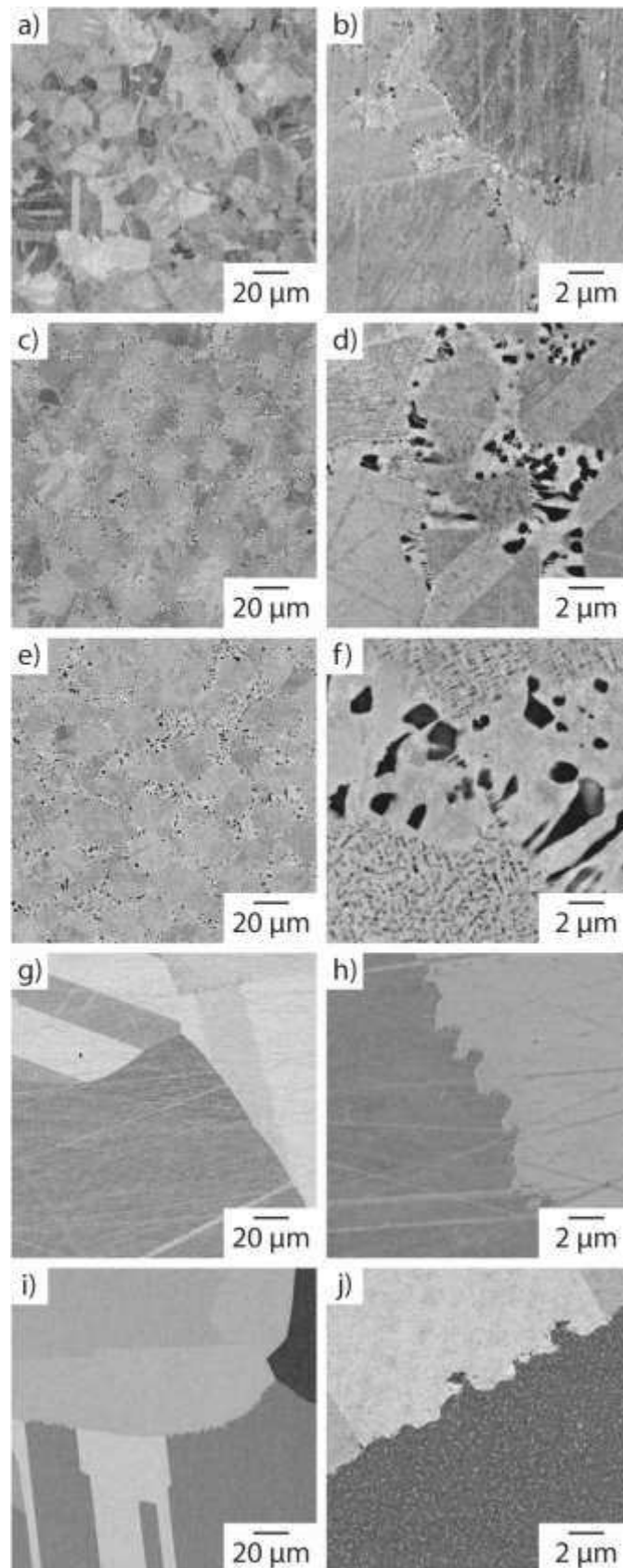
Figure 6: a) Example of X-ray diffraction pattern and Pawley analysis obtained from the sample following thermal exposure to 600°C for 100 hours. b) Evolution of the A1 and L1$_2$ lattice parameters as a function of exposure temperature and c) lattice misfit evolution as a function of exposure temperature.
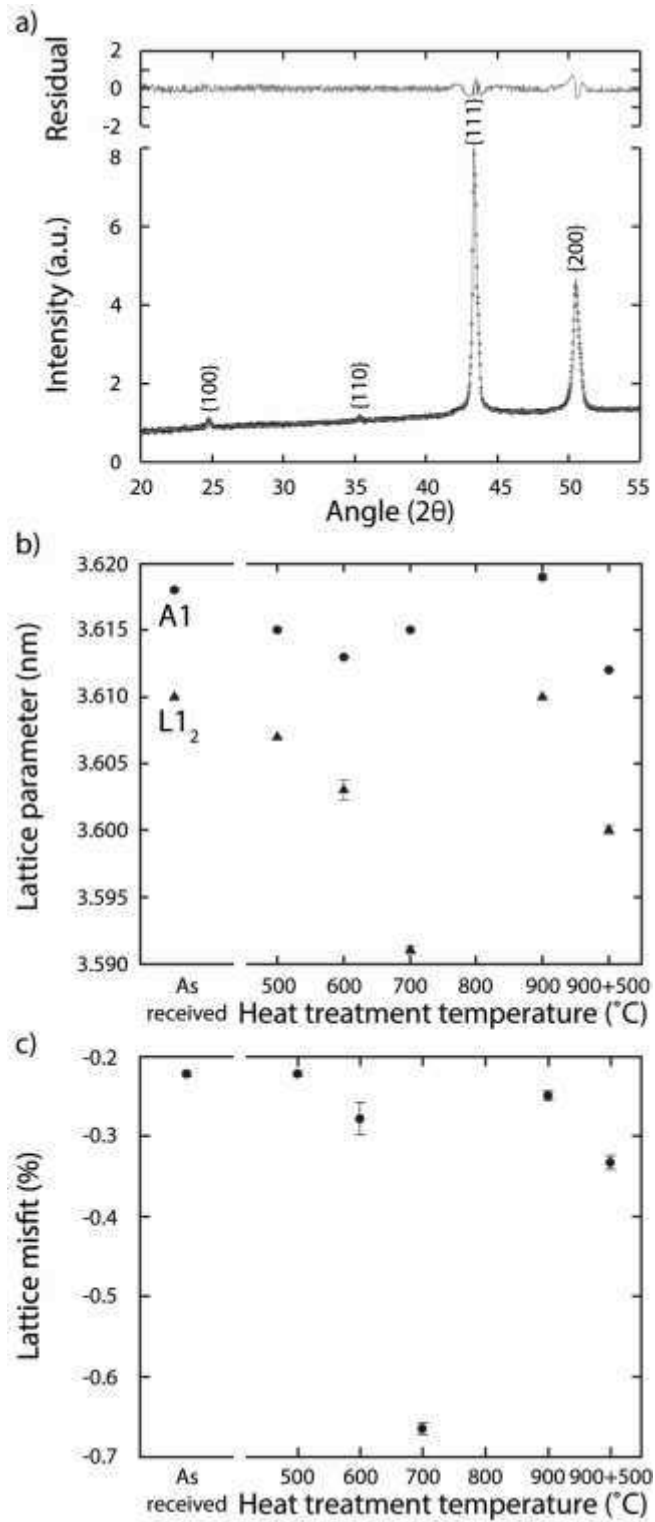
Figure 7: Vickers hardness measurements as a function of heat treatment temperature.